Effect of chemical composition on the semisolid tensile properties and hot tearing susceptibility of AA6111 DC cast alloys

Mohamed Qassem[1], Mousa Javidani[1,*] , Daniel Larouche[2], Josée Colbert[3], and X.-Grant Chen[1]

[1] *Department of Applied Science, University of Quebec in Chicoutimi, Saguenay, QC G7H 2B1, Canada*

[2] *Department of Mining, Metallurgy and Materials Engineering, Laval University, Quebec, QC G1V 0A6, Canada*

[3] *Arvida Research and Development Centre, Rio Tinto Aluminum, Saguenay, QC G7S 4K8, Canada*

ABSTRACT

The semisolid tensile properties of two AA6111 direct-chill cast alloys (A and B) have been studied. The Cu, Mn, and Si contents of alloy A are higher than those of alloy B. The microstructures of the alloys were analyzed before tensile testing and after tensile fracture. Isothermal holding was performed in the temperatures of 510, 520, 535, 552, 564 and 580 °C for 1 h to study porosity/void formation in both alloys. Tensile tests were conducted near the solidus temperature in the temperature range of 450–580 °C at a strain rate of 10^{-4} s^{-1}. The strain during tensile testing was measured using the digital image correlation method to obtain reliable stress–strain curves. The results revealed that the tensile strengths of the alloys gradually decreased to zero with increasing temperature to arrive at the zero-stress temperature, whereas the strains at the failure decreased sharply with increasing temperature until zero-ductility temperature (ZDT) was reached. Moreover, the failure strain of alloy B at any given testing temperature was higher than that of alloy A. Non-mechanical and mechanical hot-tearing criteria were used to study the hot-tearing susceptibilities (HTSs) of the alloys. Considering the mechanical criterion, the ZDT and brittle temperature range of alloy A were lower and larger than those of alloy B, respectively, indicating that the HTS index of alloy A was higher than that of alloy B.

 Springer

Introduction

Hot tearing, a common cast defect that occurs during the last stage of solidification, involves a continuous solid network of dendritic grains surrounded by a liquid film and pockets [1]. Mush structures are often subjected to tensile stress due to the thermal gradient and solidification shrinkage during casting. When the strength of the mush structure is insufficient to sustain the applied thermal stress, cast defects, such as hot tearing and porosity, occur [1–3]. Hot-tearing susceptibility (HTS) depends on several factors, such as solidification interval, microstructure development, eutectic feeding ability, and mechanical response of solidified microstructure [1–3].

The partial remelting method of as-cast samples during tensile testing has been widely adopted to investigate the mechanical response of semisolid Al alloys because it induces similar stress–strain conditions to those during solidification and provides quantitative stress and strain results for semisolid alloys [4, 5]. However, partial remelting of samples subjected to tensile tests presents some challenges, such as high thermal gradients and strain localizations, even at small strains [6]. Several researchers have investigated the semisolid tensile properties of various Al alloys, including AA5182 [7–9], AA3014, AA6111 [10], and AA6061 [11]. Previous studies have indicated that tensile tests should be performed in the strain-rates range of 10^{-5}—10^{-3} s^{-1} to simulate the direct-chill (DC) casting process [7, 12, 13]. Hot-tearing studies require semisolid tensile tests at low liquid fractions (f_L <10%), such that the specimens retain their original shapes as solid [11]. A short holding time at a semisolid temperature (within a few minutes) and high heating rates are recommended for partial remelting tests to minimize the effect of back-diffusion [4].

HTS is strongly related to the alloy composition, and the addition of small amounts of alloying elements can affect the HTS indices of Al alloys [1, 2]. Fe is usually considered a harmful element in Al–Mg–Si alloys because coarse and large Fe-rich intermetallics can hinder metal feeding during the last stage of solidification [14]. It is reported that the hot tearing susceptibility of Al–Mg-Si-Fe alloy reaches to its maximum at 0.2% Fe [15]. By adding Mn to Al–Mg-Si alloys, the Chinese-script Fe-bearing intermetallics were formed to suppress the formation of coarse β-Fe intermetallics, which facilitated the formation of solid bridges and the flow of liquid metal within semisolid structure [16]. It is also reported that increasing Si content enhanced hot tearing susceptibility, which reached to its maximum at 1% Si [17]. On the other hand, adding Cu to Al–Mg–Si alloys improves the mechanical strength of cast parts and causes the formation of Cu-bearing intermetallics (e.g., Al$_2$Cu phases) [18]. Cu-bearing intermetallics can significantly decrease the melting point and increase the solidification interval of Al alloys [18, 19]. HTS is also related to the amount of low-melting-point eutectic liquid in the later stages of solidification. Hot tear can be initiated in solid dendritic networks once the volume fraction of the liquid phase is in the range of 2–5% [20]. The relationship between the hot-tearing resistance and eutectic content depends on the distribution of the eutectic liquid to the grains [1, 21]. The formation of eutectic liquid along the grain boundaries renders the grains brittle and promotes the propagation of hot tears [22, 23].

The criteria used for predicting the HTS of Al alloys can be classified as non-mechanical and mechanical models [21, 24]. The non-mechanical criteria account for the fluid flow and healing of the structure depending on the feeding conditions. For example, Kou [25] proposed a non-mechanical model with a crack sensitivity index based on the steepness $(dT/df_s^{1/2})$ at $f_s^{1/2} \approx 1$, used to evaluate the relationship between the location of the peaks of the crack sensitivity curves and alloy chemistry. Conversely, the mechanical criteria—including stress-, strain-, and strain-rate-based models—emphasize the importance of strengths and strains developed during the interdendritic separation and bridging stages of solidification. Several hot-tearing models consider a critical temperature range, where the possibility of hot tearing increases [15, 21, 26, 27]. This temperature range, known as "brittle temperature range" (BTR), spans from the zero-ductility temperature (ZDT) to the zero-strength temperature (ZST); in this range, the material can sustain its strength without further straining [10, 28]. The wider the BTR, the larger the HTS index. The ZDTs of the alloys are typically lower than their ZSTs. The presence of minor elements, such as Cu, can significantly affect the BTR because these elements can induce a series of complex eutectic reactions toward the end of solidification [15, 29, 30].

Al–Mg–Si AA6111 wrought alloys are widely used in the transportation industry owing to their high strength/weight ratio, good corrosion resistance, and reasonable formability. AA6111 wrought alloys are primarily manufactured through ingot metallurgy via DC casting, followed by thermomechanical processes, such as rolling and extrusion. The primary alloying elements in the AA6111 alloys are Mg, Si, Cu, and Mn. Considering the multicomponent nature of the alloying elements, AA6111 alloys exhibit a wide solidification interval and generate numerous as-cast microstructures with different intermetallic phases during solidification; therefore, they are susceptible to hot tearing and porosity during DC casting. These cast defects are harmful and limit DC casting productivity.

In this study, the effect of the chemical composition of AA6111 DC cast alloys on their tensile response above the solidus temperature was studied. Considering the high sensitivity of the tensile samples to the high test temperature in the semisolid region, the strain was measured using the digital image correlation (DIC) method to ensure accurate results. HTS was further investigated using two primary criteria: a non-mechanical criterion, such as that developed by Kou [25, 31], and a mechanical criterion based on the BTR [10, 32–34].

Experimental

Materials

Two AA6111 alloys with different chemical compositions (alloys A and B) were selected, owing to their large solidification ranges (~ 142 °C based on Scheil calculations) and high HTS [10]. DC cast alloy ingots (590 mm × 185 mm × 70 mm) were provided by the Arvida Research and Development Center of Rio Tinto (Saguenay, Quebec). The chemical compositions of the alloys were determined by optical emission spectroscopy; the results are summarized in Table 1. The metallographic and tensile test samples were cut from the mid-center areas of the DC cast ingot parallel to the casting direction, as shown in Fig. 1, which well represented the bulk region in DC cast ingot.

Tensile testing near the solidus temperature

Tensile testing was conducted using a Gleeble 3800 thermomechanical testing unit with a low-force load cell at a strain rate of 10^{-4} s^{-1}. Each sample was heated to the desired temperature at a rate of 2°Cs^{-1} and maintained at the testing temperature for 60 s before tensile testing. The temperature evolution during heating and tensile testing was monitored and controlled using a K-type thermocouple spot-welded at the center of each sample. At least two tests were conducted under each condition to confirm the reliability of the results.
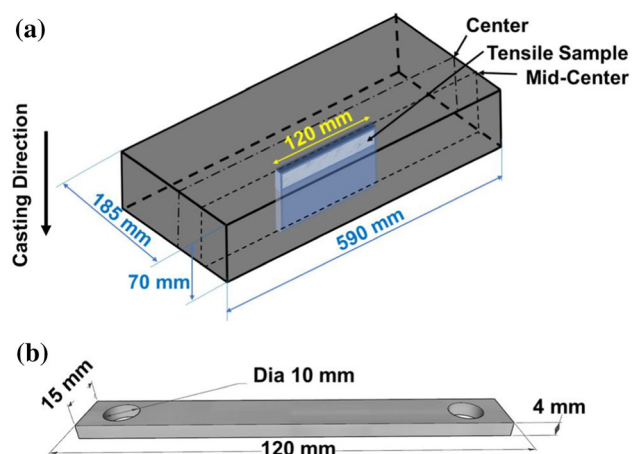
Accurate measurement of the flow stress at high temperatures was challenging because the stress of Al alloys at near-solidus temperatures was low, often ranging between 0.5 and 10 MPa. In this study, a newly developed method was used to calculate the force using the changes in L-gauge displacements [35]. This method allowed us to accurately measure the flow stress in a very narrow range and obtain consistent stress values, particularly in the semisolid state.

Strain measurements during the tensile testing were performed using the DIC method [35]. The displacement of the sample surface was monitored using a monochrome digital camera (α7RIII, Sony) mounted on a cannon tripod (Fig. 2a)) connected to a remote digital system to control the distance between the camera lens and the sample surface. A speckled pattern was created after spraying quick-dry graphite lubricant (Jig-A-Loo) onto the sample surface. The field of view on the sample surface was approximately 7.2 mm × 4.8 mm. Images were captured at a rate of 3–4 frames per second and converted to grayscale patterns of 800 × 450 pixels. Thereafter, the images were analyzed using GOM Correlate software (Germany). The parameters used for the analysis

Table 1 Chemical composition of as-received DC cast ingots

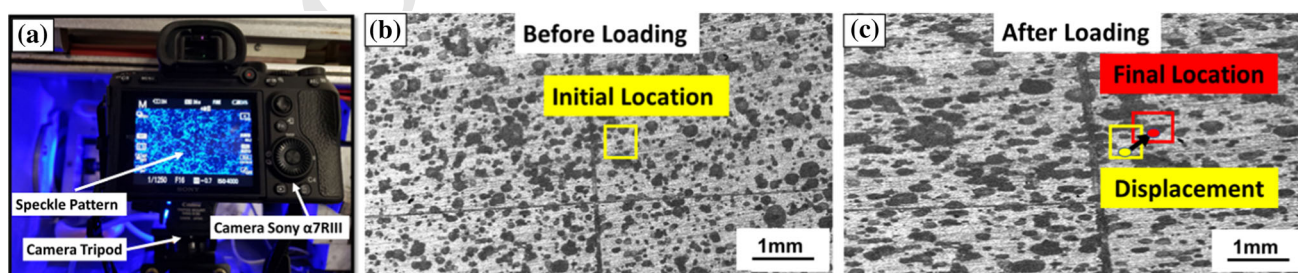| Alloy	Si	Mg	Cu	Fe	Mn	Ti
A	0.7	0.6	0.7	0.2	0.2	0.03
B	0.6	0.6	0.5	0.2	0.1	0.03
Standard AA6111	0.6–1.1	0.5–1	0.5–0.9	0.4 max	0.1–0.45	0.1 max

Figure 1 **a** Positions of metallographic and tensile samples in DC cast ingots and **b** geometry and dimension of tensile test sample.

Metallography analysis

For microstructural characterization, ingot samples were subjected to a standard metallographic polishing procedure [39]. Microstructural examinations were performed using an optical microscope and a scanning electron microscope (SEM, JSM-6480 LV) equipped with energy-dispersive spectroscopy (EDS) apparatus. Three samples sliced from the mid-center area of the ingots were used to measure the volume fractions of the different intermetallics (Fig. 1). The minimum cross-sectional area of each metallographic specimen was 160 mm^2, according to ASTM E45. Fifty images per specimen were used in this experiment. In addition, samples subjected to the tensile testing were sliced normal to the loading direction to investigate their fracture surfaces. The fractured samples were investigated in directions normal and parallel to the loading direction to study the fracture surfaces and areas surrounding the cracks. The examination of the area surrounding the crack (parallel to loading direction) can provide the details about the start of liquid film formation and fragmentation of intermetallic particles, while the cross-sectional area of fractured tensile samples (normal to loading direction) can show the initiation of the main crack responsible for the fracture.

For porosity measurements, six random samples with surface areas of 160 mm^2 were sliced from the mid-center areas of the ingots. One hundred SEM images were captured at 30 × magnification and analyzed using the ImageJ software to evaluate their porosity percentages. Six samples were sliced from the mid-center region of each ingot to study the evolution of porosity/voids at semisolid temperatures. The samples were heated isothermally in the temperatures range of 510–580 °C, followed by water quenching. Next, SEM images of the samples were

were as follow: subset size of 33 × 33, step size of 12, bicubic subpixel interpolation and resolution of 0.01 pixel or 0.09 μm. The step size is the distance between the center of the subset and the closest neighbor subset [36]. It is crucial to increase the spatial resolution of DIC by decreasing the step size to obtain an acceptable strain map for localized strain [37, 38]. The subset size was also selected to include at least three particles (Fig. 2b, c) [36, 38]. The DIC method involves comparing a reference image (before the tensile test at zero strain) with the images of the deformed samples. The measured strains were the averages of three points along the centerlines of the tensile samples, where the temperatures were the exact test temperatures. The stress–stain curves of the tensile samples were created by synchronizing the stress measured using the L-gauge method with the strain at fracture determined using the DIC method based on their evolution over time.

Figure 2 **a** Tensile test setup with the camera for 2D digital image correlation, **b** the reference image of the tensile sample surface prior to the test and **c** the deformed image during tensile test.

276 obtained at 30 × magnification. The specimens were
277 sliced 5 mm from the fracture surface parallel to the
278 loading direction to measure the porosity percentages
279 of the fractured tensile samples.

Results

Microstructure of the cast ingots

282 The as-cast microstructures of the alloys are shown in
283 Fig. 3. The microstructures of both alloys comprised
284 α-Al dendrite cells and several intermetallic phases
285 concentrated in the interdendritic regions, including
286 primary Mg_2Si, two Fe-rich intermetallics (α-Al_{15}-
287 Fe,Mn_3Si_2 and β-$Al_5(Fe,Mn)Si$), and two Cu-bearing
288 intermetallics (Q-$Al_5Mg_8Si_6Cu_2$ and θ-Al_2Cu). The
289 intermetallic phases were identified based on their
290 morphologies and SEM–EDS analysis results. The
291 dark lamellar regions in the SEM images (Fig. 3a, b)
292 are attributed to the primary Mg_2Si phase, whereas
293 the bright areas are attributed to the Fe-rich and Cu-

294 bearing phases. The morphologies and (Fe + Mn)/Si
295 ratios of the particles were used to identify the Fe-rich
296 intermetallic phases. The α-$Al_{15}(Fe,Mn)_3Si_2$ phase
297 exhibited Chinese-script morphologies, and their
298 (Fe + Mn)/Si ratios were approximately 1.5. In con-
299 trast, the β-$Al_5(Fe,Mn)Si$ phase exhibited a platelet-
300 like shape, and its (Fe + Mn)/Si ratio was found to
301 be ∼ 0.8. The results of SEM–EDS analysis showing
302 the chemical compositions of different phases are
303 listed in Table 2. The primary Mg_2Si and Al_2Cu
304 phases nucleated on the surfaces of the Fe-rich
305 intermetallics (Fig. 3c) and often grew close to the Fe-
306 rich intermetallic phases in the interdendritic region
307 (Fig. 3d).

308 The phase precipitation and temperature during
309 solidification predicted by the Scheil model for
310 AA6111 alloys were reported to be comparable to the
311 experimental values determined using two thermal
312 analysis methods [40]. Hence, the Scheil model was
313 used to estimate the solidification path and calculate
314 the fraction of the solid vs. temperature curves of the
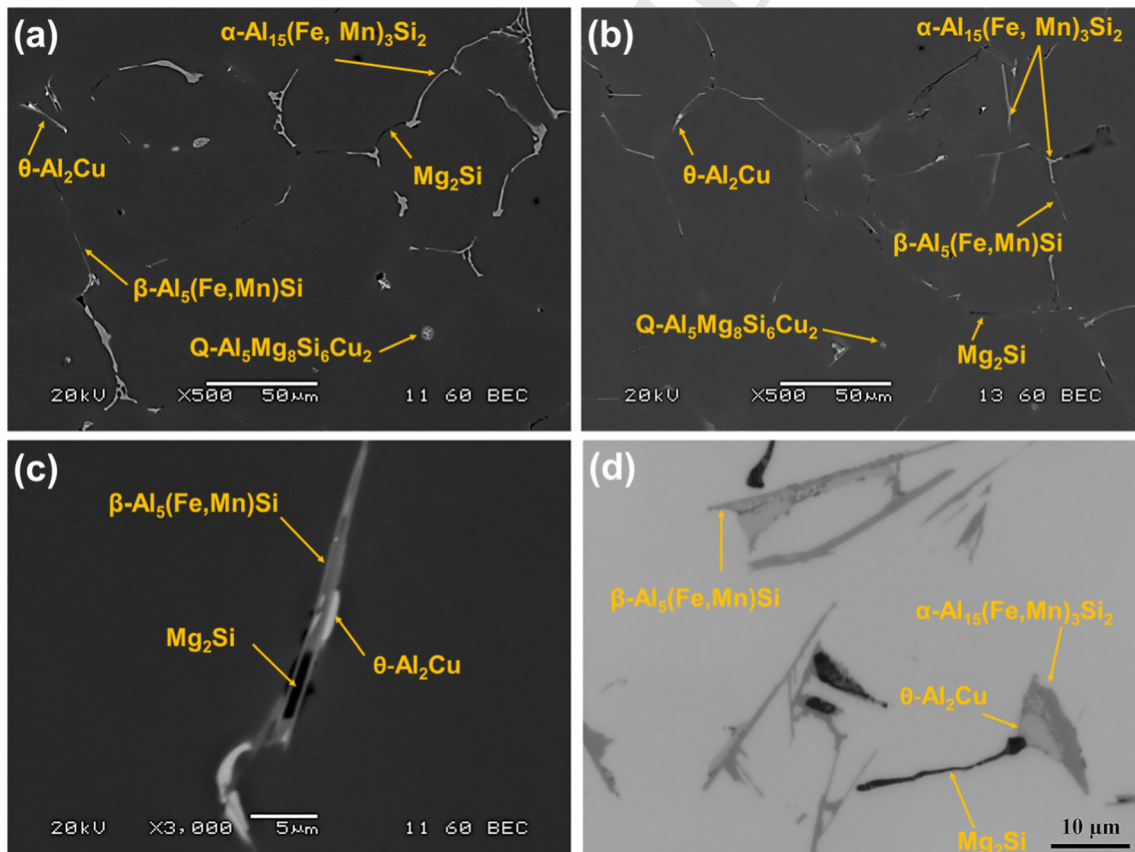
Figure 3 Microstructure of received cast ingots in the mid-center region, **a** Alloy A and **b** Alloy B, **c** Mg_2Si and Al_2Cu nucleated on Fe-rich intermetallics, and **d** presence of Mg_2Si and Al_2Cu close to Fe-intermetallic in the interdendritic region.

Springer

Table 2 The results of SEM–EDS analysis showing the chemical compositions of different phases (at%)

Phases	Al	Si	Fe	Mg	Mn	Cu	Fe + Mn/Si (at.%)
α-Al$_{15}$Fe,Mn$_3$Si$_2$	75.9	9.5	9.4	–	5.2	–	1.5
β-Al$_5$FeSi	80.9	10.6	8.2	–	0.3	–	0.8
Q-Al$_5$Mg$_8$Si$_6$Cu$_2$	67.1	12.0	–	14.4	–	6.5	–·
θ-Al$_2$Cu	81.8	–	–	–	–	18.2	–·
Mg$_2$Si	–	30.5	–	69.5	–	–	–·

alloys studied, using the Thermo-Calc software with the TCAL7 database. The results are shown in Table 3 and Fig. 4. According to the solidification path predicted by the Scheil model, after the formation of α-Al dendrites, α-Al$_{15}$(Fe,Mn)$_3$Si$_2$ precipitated at 614–617 °C, whereas β-Al$_5$(Fe,Mn)Si) precipitated at 588–594 °C. Furthermore, Mg$_2$Si was formed as the binary eutectic of α-Al + Mg$_2$Si at 555–560 °C, as well as the ternary eutectic of α-Al + Mg$_2$Si + Si at 533–536 °C. Two Cu-bearing intermetallic phases precipitated at lower temperatures, near the solidus temperature. The formation temperatures of the Q-Al$_5$Mg$_8$Si$_6$Cu$_2$ and θ-Al$_2$Cu intermetallics were 529 and 510 °C, respectively. In addition, some studies reported that the binary eutectic α-Al + α-AlFeMnSi solidified in the range of 609–634 °C [40, 41], and binary eutectic (α-Al + Mg$_2$Si) grew preferentially on the surface of β-AlFeMnSi forming a ternary eutectic (α-Al + Mg$_2$Si + β-AlFeMnSi), as shown in Fig. 3c, d [42–44].

The area fractions of the Fe-rich and Cu-bearing intermetallics in the microstructure of the two alloys were different because the Si, Cu, and Mn contents of the alloys were different. The quantitative metallographic analysis results of the alloys are shown in Fig. 5. The area fractions of Chinese-script α-Al$_{15}$(Fe,Mn)$_3$Si$_2$ of alloy A were significantly higher than those of alloy B. Adding Mn to Al alloys modifies the morphology of Fe-rich intermetallics from platelets to Chinese-script and increases the volume fraction of Fe-bearing intermetallics [45]. In contrast, platelet-like β-Al$_5$(Fe,Mn)Si is the primary Fe-rich bearing intermetallic in alloy B. The area fraction of the Fe-rich intermetallics increased from 1.4% for alloy B to 1.64% for alloy A. Furthermore, the fraction of the Mg$_2$Si phase of alloy A was greater than that of alloy B. In addition, owing to the higher Cu content of alloy A, the fraction of Cu-bearing phases in alloy A was higher than that in alloy B. In brief, the area fractions of the low-melting-point eutectic phases (Mg$_2$Si, Q, and Al$_2$Cu) of alloy A were significantly higher than those of alloy B.

## Porosity/void formation at semisolid temperatures

The porosity and void formation were studied at various temperatures in the semisolid temperature range (510–580 °C). The original porosities in the microstructures of the DC cast ingots were similar and very low (< 0.1%, Fig. 6a, b, and e). Upon increasing the temperature from 25 to 510 °C, the porosity percentage of alloy A increased from 0.08% to 0.3%, whereas that of alloy B increased from 0.07 to

Table 3 Solidification path of two alloys predicted from Scheil model and comparison with results in literature

Solidfification Path	Current study		Larouche et al. [41]		Chen et al. [40]	
	Alloy A	Alloy B	DSC	Scheil model	Thermal analysis	DSC
1. $l \rightarrow \alpha - \text{Al} + \alpha - \text{Al}(\text{Fe}, \text{Mn})\text{Si}$	616.5	614.7	621–632	630–634	609–632	633
2. $l + \alpha - \text{Al}(\text{Fe}, \text{Mn})\text{Si} \rightarrow \alpha - \text{Al} + \beta - \text{Al}(\text{Fe}, \text{Mn})\text{Si}$	588.5	594.7				606
3. $l \rightarrow \alpha - \text{Al} + \text{Mg}_2\text{Si}$	555.5	560	545–548	541–547	553–555	557
4. $l \rightarrow \alpha - \text{Al} + \text{Mg}_2\text{S} + \text{Si}$	533	536				
5. $l \rightarrow \alpha - \text{Al} + \text{Q} - \text{Phase}$	529	529	527–538	537		
6. $l \rightarrow \alpha - \text{Al} + \text{Q} - \text{Phase} + \theta - \text{Al}_2\text{Cu} + \text{Si}$	510	510	507–515	510	506	508
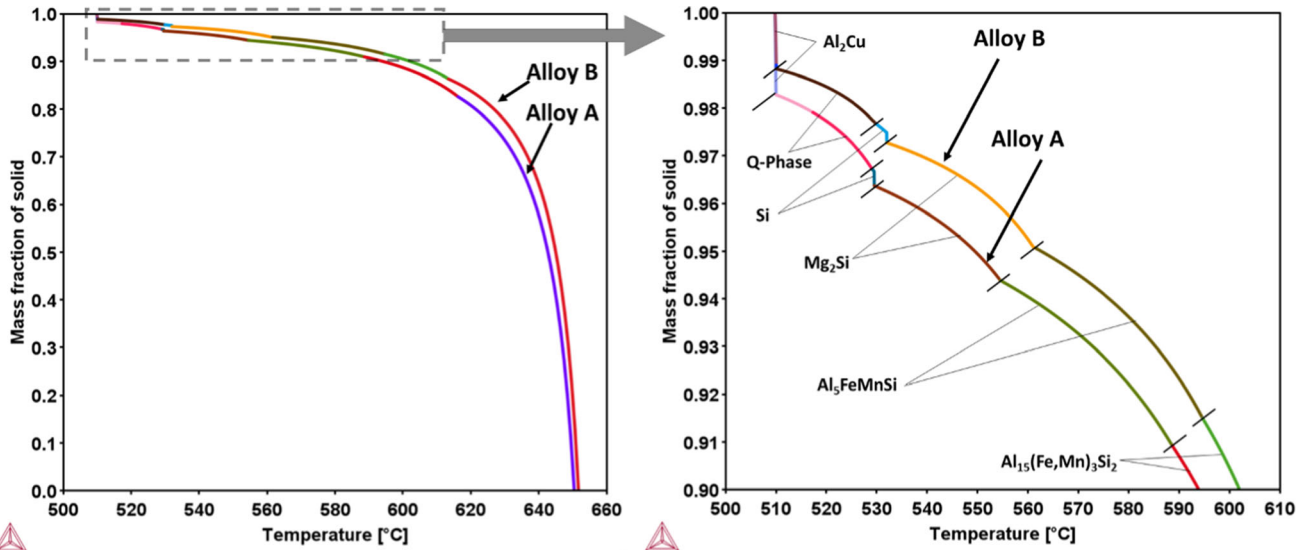
Figure 4 Evolution of mass solid fraction during solidification of both alloys calculated by the Scheil model.
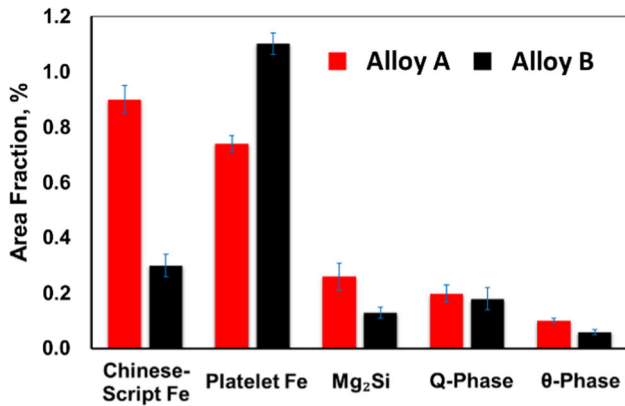
**Figure 5** Quantitative results of the area fractions of different intermtallic phases in two alloys.

0.12% (Fig. 6c, d, and e). The increase in porosity percentage and void interlinking degree were more significant for alloy A than for alloy B. The increase of the 0.05% porosity content in alloy B corresponded well with the content of Al_2Cu (i.e., 0.06%) of the sample. However, for the alloy A, the porosity was increased by (0.22%), which was higher than the Al_2Cu content of the sample. The significant increase in porosity content in alloy A implies that the Q-phase started to melt at such temperature, and therefore, the void interlinking is more significant in alloy A (Fig. 6c). Upon further increasing the temperature to the upper semisolid range (580 °C), the highest temperature for the tensile tests, the porosity percentage increased gradually with temperature for both alloys. However, the porosity of alloy A was

significantly higher than that of alloy B over the entire temperature range, attributed to higher amounts of low-melting-point eutectic phases (e.g., Mg_2Si, Q, and Al_2Cu) in the as-cast microstructure of alloy A than in alloy B. In addition, at semisolid temperatures, the porosity of alloy A became irregular along the dendrite boundaries and shrinkage-like pores formed (Fig. 6c). In contrast, the pores of alloy B increased in size without forming shrinkage-like pores (Fig. 6d). The high number of pores and changes in the porosity morphology of alloy A at high semisolid temperatures, in the absence of external tensile forces, suggest that alloy A is highly sensitive to hot-tearing evolution.

Mechanical properties at near-solidus temperature

Engineering stress–strain curves

The typical engineering stress–strain curves of alloys A and B were obtained in the temperature range of 450–580 °C and a strain rate of $\sim 10^{-4}$ s^{-1} (Fig. 7). The results of the test conducted at 450 °C were used to represent the solid-state tensile flow behavior of the alloys. In general, the flow stress increased sharply toward the peak stress. After reaching the peak stress, the flow stress progressively decreased to the fracture point (Fig. 7a). The solid-state strength and ductility of alloy A were higher and lower, respectively, than those of alloy B, attributed to the content
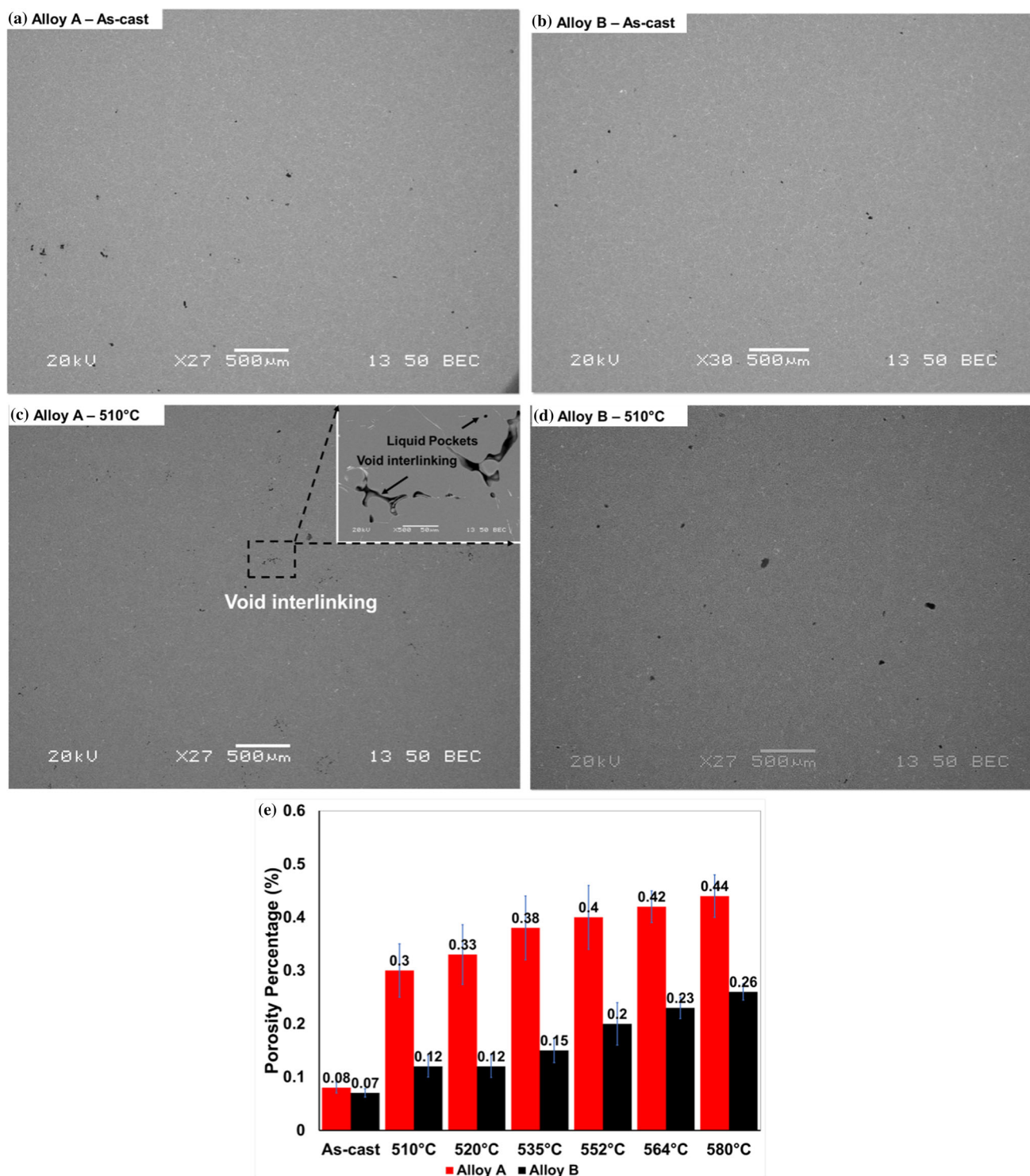
Figure 6 **a** As-cast porosity in alloy A, **b** as-cast porosity in alloy B, **c** porosity and voids in alloy A at 510 °C with a enlarged view in the inset, **d** porosity and voids in alloy B at 510 °C and **e evolution of porosity with increasing temperature in both alloys**.

of intermetallic phases, comprising Fe-rich and Cu-bearing intermetallics. The Mg_2Si phase of alloy A was higher than that of alloy B. Upon increasing the temperature to 510 °C (near the solidus temperature), both alloys exhibited plateaus in stress after reaching the peak stress, continuing until the fracture point was reached. The ductility of alloy A remained lower than that of alloy B.
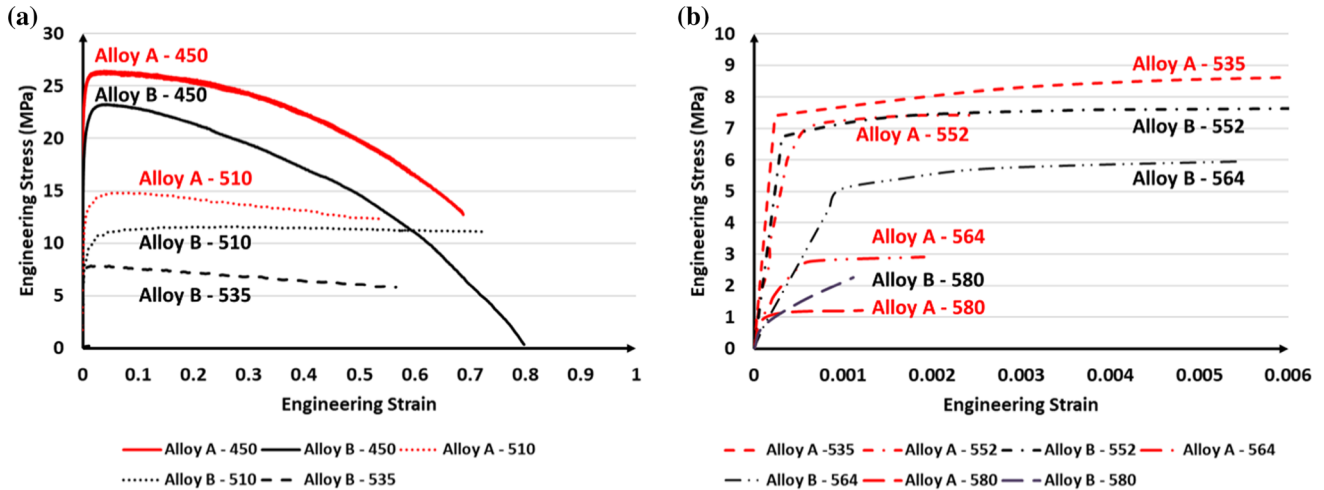
Figure 7 Engineering stress–strain curves for two AA6111 alloys **a** at 450–535 °C and **b** the enlarged view at the low strain for the temperatures between 535 and 580 °C.

Upon increasing the temperature to 535 °C, the ductility (strain at failure) of alloy A decreased sharply (3.2%), whereas alloy B exhibited a significantly greater strain at failure (approximately 60%) than alloy A (Fig. 7b). Moreover, the tensile strengths of the alloys were similar at 552 °C; however, the ductility of alloy B (2.8%) was considerably higher than that of alloy A (0.25%). All tensile properties are summarized in Table 4.

For a given mass fraction of liquid, for instance at an f_L of 4%, the strength of the mush structure of alloy A reached its maximum value much faster than that of alloy B; however, the strain at failure of alloy A was lower than that of alloy B (Fig. 8). The area under the engineering stress–strain curve of a material is equivalent to the modulus of toughness, representing the strain energy per unit volume required to fracture the material [46]. The higher the absorbed energy required for crack growth, the larger the stored strain energy [47, 48]. Accordingly, at f_L = 4%, the resistance of alloy B to crack propagation was
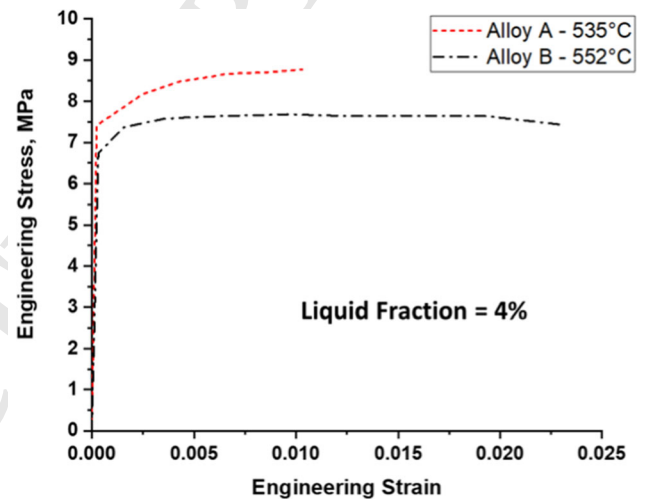
Figure 8 Engineering stress–strain curves for two AA6111 alloys at a constant liquid fraction of 4%.

significantly higher than that of alloy A (the strain energy of alloy B (0.172 MJm^{-3}) was higher than that of alloy A (0.086 MJm^{-3})).

Table 4 Tensile properties of alloys A and B over the whole temperature range

| Temperature, °C	Ultimate tensile strength, MPa		Failure strain, %	
	Alloy A	Alloy B	Alloy A	Alloy B
450	26.30 ± 0.80	23.30 ± 0.90	69.30 ± 5.20	80.30 ± 4.20
510	20.40 ± 0.90	16.40 ± 0.80	61.10 ± 4.12	76.20 ± 5.10
535	15.60 ± 0.50	12.50 ± 0.90	3.20 ± 0.20	67.80 ± 3.62
552	7.40 ± 0.30	7.70 ± 0.70	2.50 ± 0.15	2.80 ± 0.20
564	2.90 ± 0.40	5.90 ± 0.60	1.80 ± 0.02	0.50 ± 0.02
580	1.20 ± 0.30	2.30 ± 0.20	0.10 ± 0.01	0.10 ± 0.01

Strain field at fracture zone

The strain maps of alloys A and B with the same f_L of 4% are presented in Fig. 9. The strain distribution along the sample length indicated that the location of the maximum strain for alloy A was random, and the peak strain appeared away from the sample center ($\sim$ 2 mm). Crack opening is expected to occur in the hotspot zone, where the strain should be maximum [35]. In other words, cracking should be located at the centerline where the temperature is the highest. However, for crack-susceptible alloys, the hot tear can be initiated at the weakest points of the sample (e.g., porosity and voids). Therefore, the initiation outside the hotspot zone for alloy A was attributed to pre-existing defects promoting strain accumulation [49]. The maximum strains at fracture for alloys A and B are 3.2% and 3.8%, respectively. As the f_L values of both alloys were the same, alloy A, which fractured at a lower strain, was more sensitive to pre-existing defects than alloy B.

Figure 10 shows the time evolution of the strain for the two alloys at two f_L values. As shown, the strain rates of the alloys were considerably different. For a f_L of 4%, after 15 s, the strain of alloy A reached a maximum of 3.2%, whereas that of alloy B reached only 0.5% (compared with its total strain of 3.82%). The strain rate of alloy A was considerably much higher than that of alloy B. After 11 s of tensile testing, the strain of alloy B approached 0%, whereas that of alloy A was approximately 0.35%. In addition, alloy A exhibited a steep increase in strain near the fracture point, whereas alloy B exhibited a gradual increase in strain until the fracture point. The higher strain rate of alloy A was attributed to its greater sensitivity to hot tearing.

Figure 10a shows the strain rate of alloy A remained unchanged with increasing temperature from 535 to 552 °C, whereas its strain at failure decreased significantly. It was also found that alloy B exhibited higher failure strain compared with alloy A at a constant mass fraction of liquid (i.e., 4%f_L). The enlarged view of the strain evolution at the early stage of the curves (i.e., time $\leq$ 10 S) is presented in Fig. 10b. At 552 °C, the strains (ε) and strain rates ($\dot{\varepsilon}$) AQ4 of the alloys at the same strength were significantly different; moreover, alloy A fractured before strain localization began in alloy B, indicating that the cracks were propagated in alloy A even prior to initiation of the cracking in alloy B.
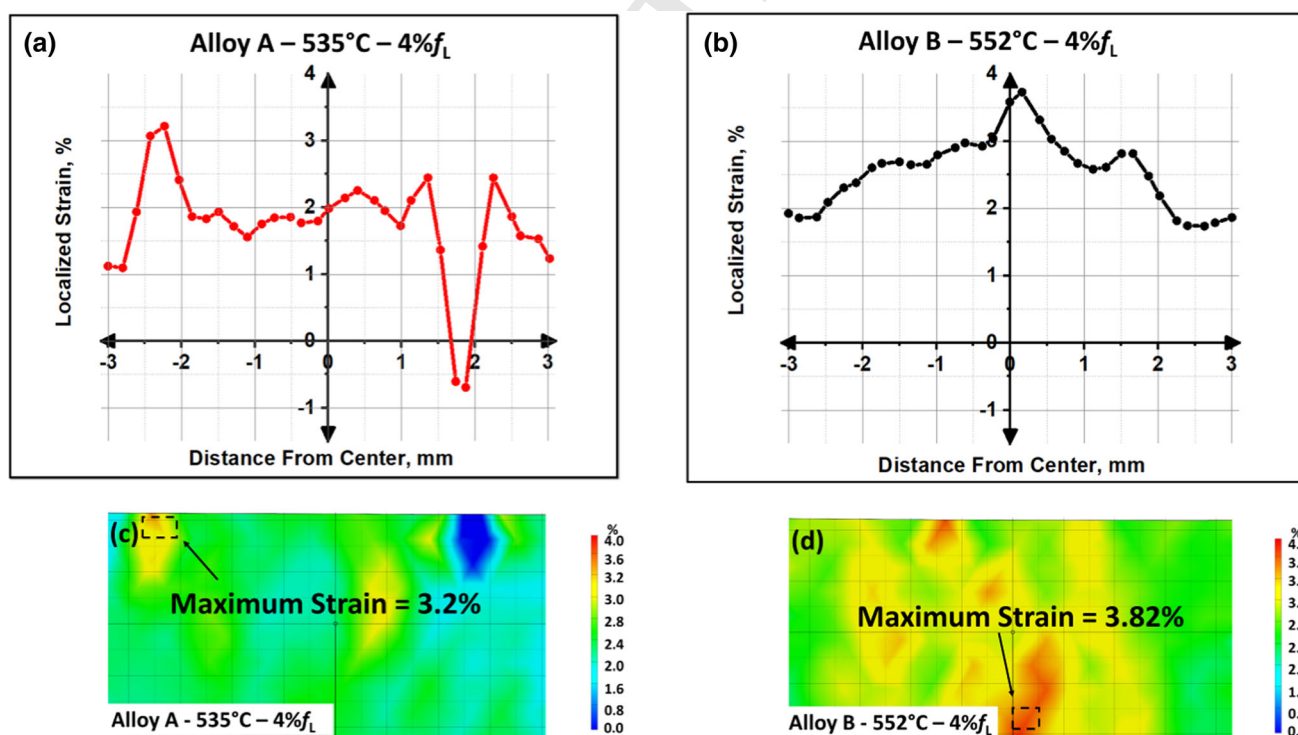
Figure 9 Strain fields and maps at a constant liquid fraction (4%), **a**, **c** Alloy A, **b**, **d** Alloy B, **a**, **b** strain distribution along sample lengthwise direction before fracture, and **c**, **d** strain map showing strain contours before fracture.

Figure 10 a The strain evolution for alloys A (dashed line) and B (solid line) with time, and **b** enlarged view of the rectangular area indicated in Fig.a.
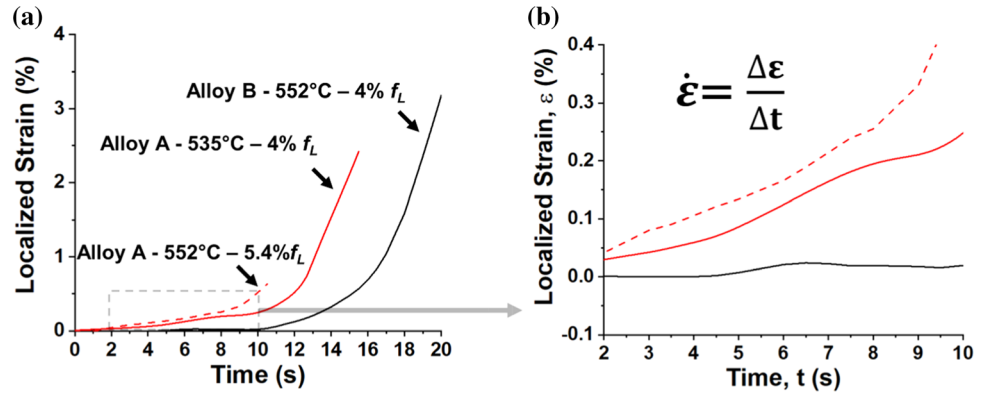

Fracture surface analysis

Figure 11 shows the area normal to the fracture surfaces of the tensile samples tested at 510 °C (the solidus temperature). The liquid pockets formed in the microstructure at 510 °C (Fig. 6) were transformed into large voids, indicating that the fracture mechanism was based on void coalescence. As mentioned in Sect. 3.2, shrinkage porosity and voids were readily formed in alloy A at this temperature. By measuring the porosity percentage of the fractured tensile samples of both alloys, the porosity percentage of alloy A (0.65%) was higher than that of alloy B (0.5%). Void coalescence was also more significant in alloy A, with the maximum void size of 280 μm; in contrast, the maximum void size of alloy B was only 80 μm. As mentioned in Sect. 3.2, the susceptibility of alloy A to the porosity formation during isothermal holding was higher than that of alloy B. Therefore, during heating to 510 °C, followed by the subsequent isothermal holding before tensile testing,

shrinkage pores formed in alloy A; therefore, voids grew faster in alloy A than in alloy B.

Figure 12 shows the starting points of liquid film formation via coalescence the pre-existent liquid pockets for both alloys. By investigating the fractured tensile sample of alloy A at 535 °C, a liquid film with a significant width started to develop (Fig. 12a, b). Conversely, the liquid pockets in alloy B started to coalesce, forming intergranular cracks or shrinkage porosity at 535 °C (Fig. 12c and d). No traces of liquid film were present in the cracks, suggesting that the intergranular liquid films were very thin. Moreover, liquid pockets were distributed along the Fe-rich intermetallics. Upon further increasing the temperature from 535 to 552 °C, the liquid films were distributed along the grain boundaries of alloy B (Fig. 12e, f). The width of the liquid film of alloy B at 552 °C (4.95 μm) was approximately two times larger than that of alloy A at 535 °C (2.15 μm). As the width of the liquid film for alloy A was smaller, more bridges readily formed across the cracks by the Fe-rich intermetallics and Mg_2Si phase (Fig. 12b). Large
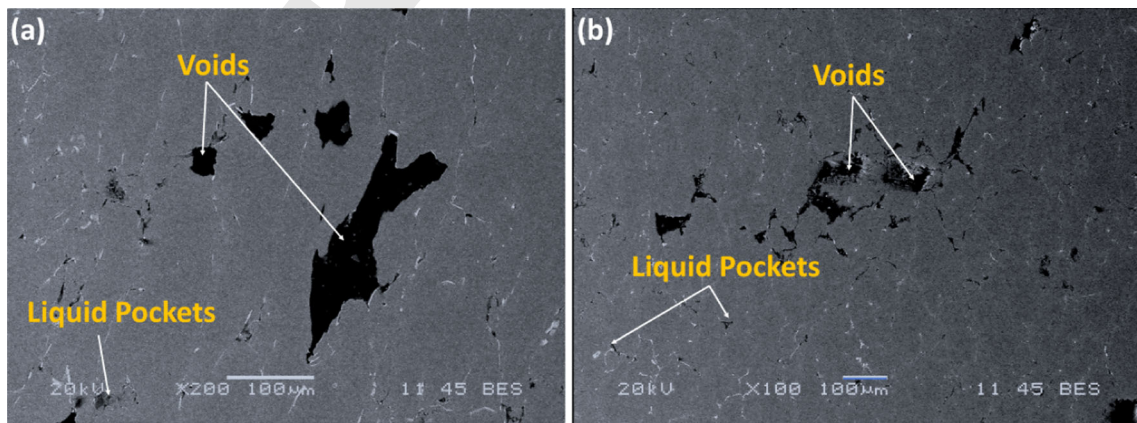

Figure 11 Appearance of liquid pockets in samples tested at 510 °C: **a** alloy A and **b** alloy B.
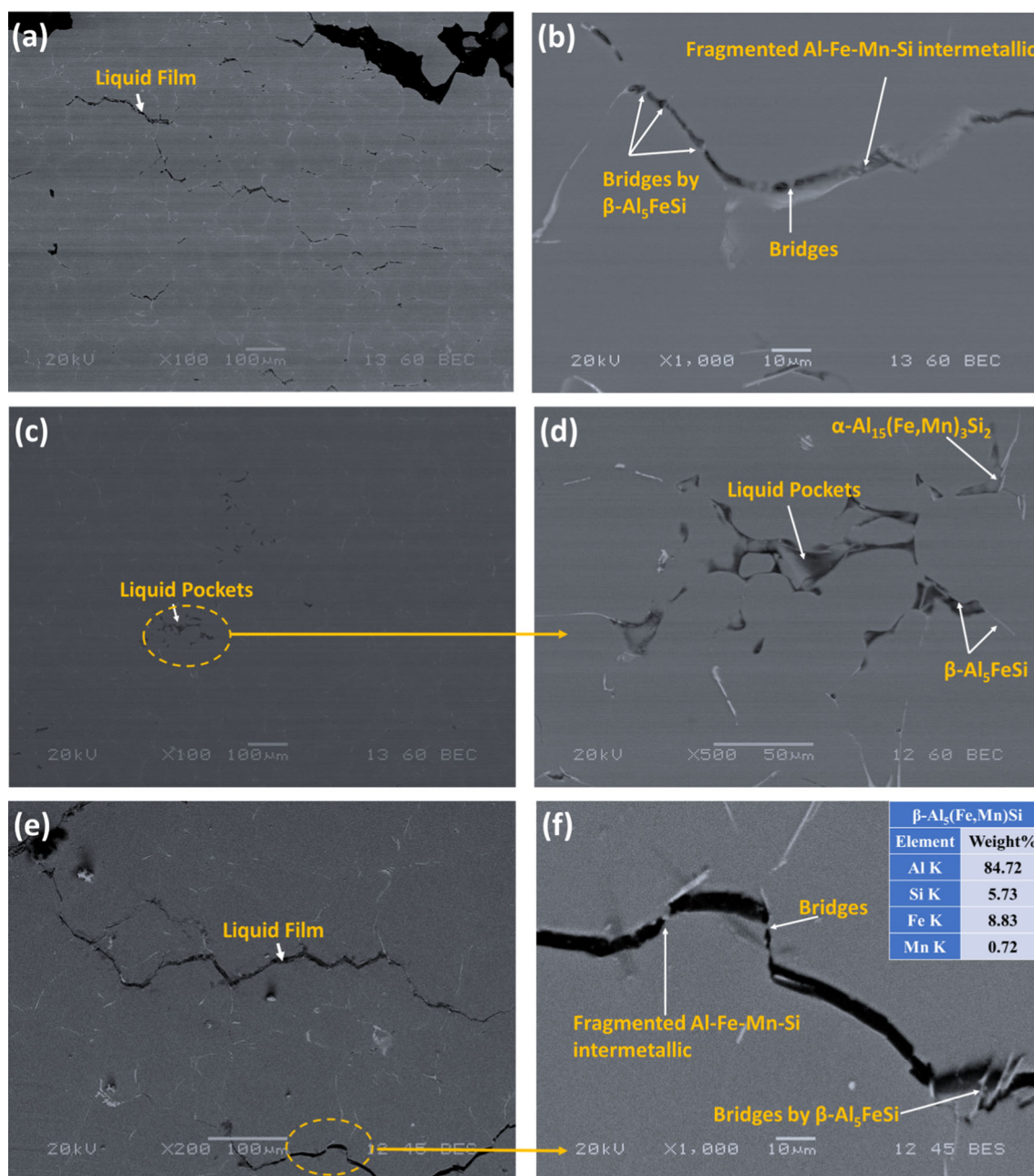
Figure 12 Appearance of liquid film along grain boundaries at 4% f_L for **a**, **b** alloy A tested at 535 °C, **c**, **d** the coalescence of liquid pockets forming cracks in alloy B at 535 °C, and **e**, **f** alloy B tested at 552 °C.

534 platelet-like Fe-rich intermetallics formed bridges in
535 the alloy B, whereas small fragmental Fe-rich inter-
536 metallics formed bridges in the alloy A (Fig. 12b and
537 f). The small width of the liquid films of alloy A
538 facilitated the formation of solid bridges by the small
539 Fe-rich intermetallics. It was expected that the small
540 fragments of Fe-intermetallics would stop forming
541 bridges upon a further increase in liquid film width
542 with increasing temperature.

543 The fracture surfaces of alloys A and B at 580 °C
544 are presented in Fig. 13. At this temperature, both the
545 alloys exhibited low strength and ductility. The
546 fractured bridges observed on the fracture surface of
547 alloy A—marked by arrows in Fig. 13a—indicate that
548 the intermetallics could not sustain the strength of the
549 mush structure at temperatures in this range. Fur-
550 thermore, the Fe-rich intermetallics were mostly
551 fragmented and could not sustain the strength of the
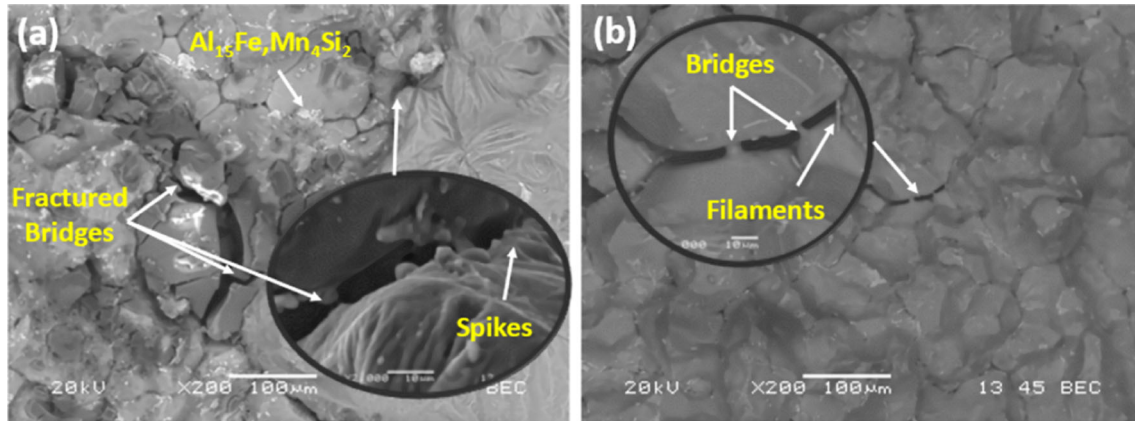
Figure 13 Fracture surface of samples tested at 580 °C for **a** Alloy A and **b** Alloy B.

specimens. In addition, the liquid film thickening of alloy A was more severe than that of alloy B because the strength of alloy A decreased considerably faster (Fig. 7b). The width of the liquid film of alloy A increased to 6.6 μm, with Fe-rich intermetallics no longer able to form intact solid bridges. The spikes observed around the fractured bridges are attributed to the extremely localized ductility of alloy A.

Nevertheless, alloy B retained its strength, even at 580 °C. The width of the liquid film of alloy B did not change significantly at 580 °C (5.3 μm). The small width of the liquid film facilitated bridge formation, and the presence of an unbroken platelet-like β-AlFeMnSi phase (Fig. 13b) increased the sample strength and delayed crack propagation.

Discussion

The microstructures and mechanical responses of AA6111 DC cast alloys (A and B) in the semisolid state at high f_s values were significantly different. Two criteria were used to study the HTS behavior of the alloys. The first, based on a non-mechanical criterion proposed by Kou [25, 31] and modified by Hu et al. [50], was introduced to establish a relationship between HTS and the chemical compositions of the alloys. This criterion is based on the evolution of the solid fraction with temperature during the late stage of solidification. The second criterion is based on a mechanical model used to identify the BTR of the alloys [10, 32, 34]. The semisolid behaviors and HTS indices of the alloys were analyzed using these **AQ6** approaches.

Non-mechanical criterion

Kou used the the crack sensitivity factor $(dT/df_S^{1/2})$ value near $(f_S)^{1/2} = 1$ to evaluate the HTS behavior of alloys with columnar grain structures [25, 51]. Hu et al. [50] subsequently modified the model, as $dT/df_S^{1/3}$ near $(f_S)^{1/3} = 1$, to predict the HTS behaviors of alloys with equiaxed grain morphology. Hu's model was used because the grain structures of alloys A and B were equiaxed. According to Kou, the predicted results for peak crack susceptibility (Λ-shaped curve) in the solidification range of $0.87 < f_S < 0.94$ were consistent with the experimental results [25, 31]. For example, in Al–Si alloys, peak crack susceptibility occurred at a Si content of 1%, consistent with the hot-tearing data of Al–Si alloys reported by Singer [17] and Vero [52]. Therefore, this solidification range was adopted in this study. The T vs. $(f_S)^{1/3}$ curves for alloys A and B are shown in Fig. 14a. The calculated hot-tearing index $(\Delta T/\Delta f_S^{1/3})$ of alloys A and B were 1900 and 1540 °C, respectively (Fig. 14b). The pre-**AQ7**dicted higher HTS of alloy A is partially attributed to its higher Cu content. Furthermore, the HTS indices of Al–Mg–Si–Cu alloys increase with increasing Cu content [53, 54].

The primary drawback of these HTS models is the lack of a theoretical basis for selecting a specific f_S range; hence, the accuracy of the predicted results depends significantly on the selected f_S range [25, 50]. In addition, back-diffusion considerably affects the high-crack-susceptibility region [31]. As back diffusion was not considered in these models, the HTS behavior of the alloys was further investigated using the mechanical criterion.
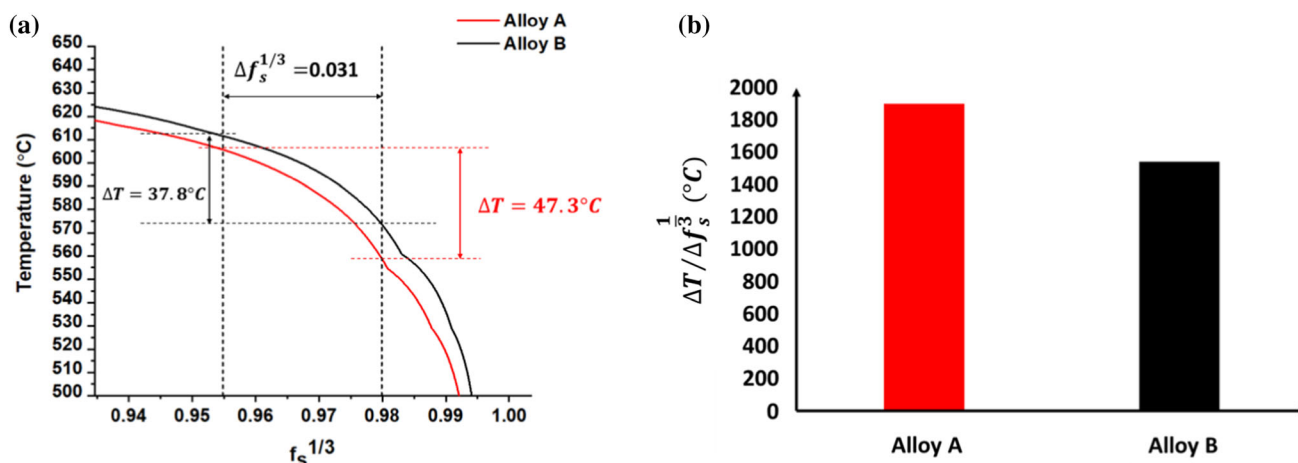
Figure 14 Prediction of HTS of two AA6111 alloys based on steepness of T versus $(f_S)^{1/3}$ curves: **a** T versus $(f_S)^{1/3}$ curves in the f_S range of 0.87–0.94 ($0.955 < (f_S)^{1/3} < 0.98$); **b** the difference of hot tearing index between alloys A and B.

Mechanical criterion

The relationship between the ultimate tensile strength (σ_{uts}) and true failure strain (ε_f) of the alloys with temperature and f_S is presented in Fig. 15. Three zones were observed in the failure strain behavior of the alloys over the studied temperature. The first zone ranges from the completely solid-state to 525 °C (Fig. 15a). Throughout this zone, σ_{uts} and ε_f decreased gradually, and the alloys exhibited a ductile behavior. Upon further increasing the temperature, a transition zone emerged, where the alloy ductility decreased abruptly. At the end of this zone, the ductility reached a very low value, and the corresponding temperature is known as ZDT. It has been proposed that ZDT corresponds to the temperature at which the strain is lower than 3% [55]. Therefore, the ZDTs of alloys A and B were determined to be 535 and 552 °C, respectively (Fig. 15b). The ZDTs of both the alloys corresponded to the same f_s value of 0.96. ZDTs of AA6111 alloys have been reported to occur at $f_s = 0.95$ [6, 7]. However, Phillion et al. [10] demonstrated that the ZDT highly depended on the solidification sequence and the corresponding alloy composition, reporting that the ZDTs of AA6111 alloys occurred at $f_s = 0.99$. The third zone, known as the BTR, is located above the ZDT and extends to a temperature at which the strengths of the alloys approach zero, known as the ZST. The ZSTs of alloys A and B were estimated to be ~ 590 °C (Fig. 15a),
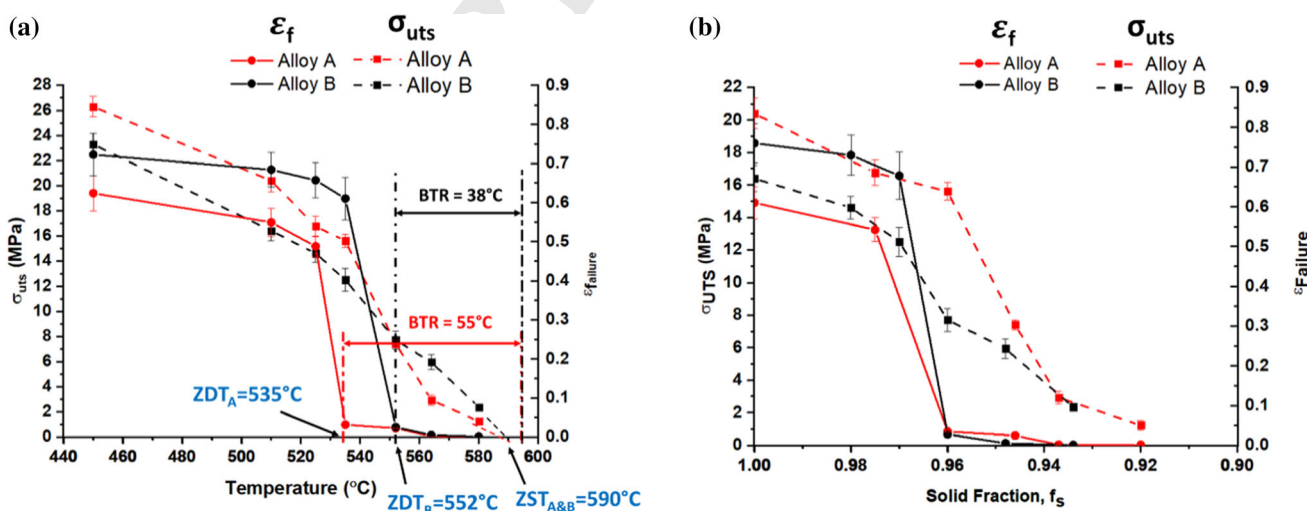
Figure 15 The UTS (σ_{uts}) and failure strain (ε_f) **a** as a function of temperature and **b** as a function of solid fraction for two semisolid AA6111 alloys.

and the corresponding f_S values of alloys A and B, at which the ZST was reached, were estimated to be at approximately 0.92 and 0.91, respectively (Fig. 15b).

Throughout the first zone (gradual decrease in ductility) and above the solidus temperature, liquid pockets began to form in the alloys due to the melting of the Cu-bearing low-melting-point eutectic phases. Moreover, individual liquid pockets were randomly distributed in the microstructures of the alloys (Fig. 11). In the second zone, the liquid pockets began to interlink and coalesce, causing a significant decrease in ductility. The ZDT was reached at the end of this zone as continuous liquid films started to form along the grain boundaries (Fig. 12e and f).

As previously mentioned, the BTR zone ranged from ZDT to ZST; ZST corresponds to the intergranular separation stage. Phillion et al. [10] determined that the ZST of an AA6111 alloy pulled at a strain rate of 10^{-4} s^{-1} was 580 °C, comparable to that estimated in this study (590 °C). Accordingly, the BTRs of alloys A and B were calculated to be 55 and 38 °C, respectively (Fig. 15a). Throughout the BTR, the widths of the liquid films along the grain boundaries, separation of the bridges across cracks, and fragmentation of Fe-intermetallics increased (Fig. 13). The formation of continuous liquid films significantly decreased the interfacial energy at the solid–liquid interface, facilitating crack propagation and hot tearing [21]; therefore, the larger the BTR, the larger is the HTS index [10]. The strength of alloy A decreased faster than that of alloy B throughout the BTR zone, as indicated by the dashed vertical lines in Fig. 15a. Furthermore, the strength of alloy A was low (< 1 MPa) at 580 °C, whereas that of alloy B was relatively high (> 2 MPa). The solid bridges in alloy A were broken at 580 °C; however, the solid bridges formed by Fe-rich AlFeMnSi intermetallics persisted in alloy B (Fig. 13).

Conclusions

The semisolid tensile properties at high solid fractions of two AA6111 DC cast alloys with different chemical compositions were investigated. The Cu, Mn, and Si contents of alloy A were higher than those of alloy B. Based on microstructure and semisolid tensile results, the non-mechanical and mechanical criteria were used to investigate the HTS behaviors of the alloys. The results indicated that the HTS index of alloy A was higher than that of alloy B. The following conclusions were drawn:

1. The incipient melting of the Cu-bearing and Mg_2Si intermetallics during isothermal heating near and above the solidus temperature (i.e., in the range of 510–580 °C) caused a sharp increase in porosity/void formation, thus promoting void growth during tensile testing in the semisolid state. The fracture mechanism of the tensile samples involved void coalescence, which developed along various intermetallics. As the amount of low-melting-point eutectic phases (e.g., Mg_2Si, Q, and Al_2Cu) in the as-cast microstructure of alloy A was higher than that of alloy B, the enhanced porosity formation and void interlinking in alloy A were more significant than those in alloy B.

2. The tensile strength of both alloys decreased gradually with increase in temperature, reaching similar values at 552 °C. At temperatures above 552 °C, the decrease in strength of alloy A was more significant than that of alloy B. The ε_f values of the alloys decreased sharply with increasing temperature until ZDT was reached; the ZDT of alloy A (535 °C) was lower than that of alloy B (552 °C). At temperatures lower than the ZDT, the ε_f values of alloy B were higher than those of alloy A.

3. According to the non-mechanical criterion, the $dT/df_S^{1/3}$ values of alloy A in the f_s range of 0.87–0.94 were higher than those of alloy B; therefore, the HTS index of alloy A was higher than that of alloy B.

4. According to the mechanical criterion and using the ZDT and ZST concepts, the BTR values of alloys A and B were calculated to be 55 and 38 °C, respectively. In addition, alloy A exhibited a sharper decrease in strength in the BTR zone than alloy B. The wider BTR (45%) and lower strength of alloy A, associated with significant liquid film thickening and fragmentation of Fe-rich intermetallics, indicated that its HTS was higher than that of alloy B.

Acknowledgements

Journal : **10853 - Large 10853**	Dispatch : **18-11-2022**	Pages : **18**
Article No. : **7960**	☐ LE	☐ TYPESET
MS Code : **JMSC-D-22-03589R1**	☑ CP	☑ DISK

🖄 Springer

References

[1] Li S, Apelian D (2011) Hot tearing of aluminum alloys. Int J Met 5:23–40. https://doi.org/10.1007/bf03355505

[2] Eskin DG, Suyitno L (2004) Katgerman, mechanical properties in the semi-solid state and hot tearing of aluminium alloys. Prog Mater Sci 49:629–711. https://doi.org/10.1016/S0079-6425(03)00037-9

[3] Eskin DG (2008) Direct chill casting: development of the technology. In: Eskin DG (ed) Physical metallurgy of direct chill casting of aluminum alloys. CRC Press, Boca Raton, pp 1–18. https://doi.org/10.1201/9781420062823.ch1

[4] Han Q, Hassan MI, Viswanathan S, Saito K, Das SK (2005) The reheating-cooling method: a technique for measuring mechanical properties in the nonequilibrium mushy zones of alloys. Metall Mater Trans A Phys Metall Mater Sci 36:2073–2080. https://doi.org/10.1007/s11661-005-0328-4

[5] Bolouri A, Liu K, Chen XG (2016) Effects of iron-rich intermetallics and grain structure on semisolid tensile properties of Al-Cu 206 cast alloys near solidus temperature. Metall Mater Trans A Phys Metall Mater Sci. 47:6466–6480. https://doi.org/10.1007/s11661-016-3744-8

[6] Phillion AB, Cockcroft SL, Lee PD (2008) A new methodology for measurement of semi-solid constitutive behavior and its application to examination of as-cast porosity and hot tearing in aluminum alloys. Mater Sci Eng A 491:237–247. https://doi.org/10.1016/j.msea.2008.01.078

[7] Colley LJ, Wells MA, Maijer DM (2004) Tensile properties of as-cast aluminum alloy AA5182 close to the solidus temperature. Mater Sci Eng A 386:140–148. https://doi.org/10.1016/j.msea.2004.07.019

[8] Van Haaften WM, Kool WH, Katgerman L (2002) Hot tearing studies in AA5182. J Mater Eng Perform 11:537–543. https://doi.org/10.1361/105994902770343791

[9] Van Haaften WM, Magnin B, Kool WH, Katgerman L (2002) Constitutive behavior of as-cast AA1050, AA3104, and AA5182. Metall Mater Trans A Phys Metall Mater Sci 33:1971–1980. https://doi.org/10.1007/s11661-002-0030-8

[10] Phillion AB, Thompson S, Cockcroft SL, Wells MA (2008) Tensile properties of as-cast aluminum alloys AA3104, AA6111 and CA31218 at above solidus temperatures. Mater Sci Eng A 497:388–394. https://doi.org/10.1016/j.msea.2008.07.027

[11] Giraud E, Suery M, Coret M (2010) Mechanical behavior of AA6061 aluminum in the semisolid state obtained by partial melting and partial solidification. Metall Mater Trans A Phys Metall Mater Sci 41:2257–2268. https://doi.org/10.1007/s11661-010-0268-5

[12] Lahaie DJ, Bouchard M (2001) Physical modeling of the deformation mechanisms of semisolid bodies and a mechanical criterion for hot tearing. Metall Mater Trans B Process Metall Mater Process Sci 32:697–705. https://doi.org/10.1007/s11663-001-0124-5

[13] Ludwig O, Drezet JM, Ménésès P, Martin CL, Suéry M (2005) Rheological behavior of a commercial AA5182 aluminum alloy during solidification. Mater Sci Eng A 413–414:174–179. https://doi.org/10.1016/j.msea.2005.09.087

[14] Javidani M, Larouche D (2014) Application of cast Al–Si alloys in internal combustion engine components. Int Mater Rev 59:132–158. https://doi.org/10.1179/1743280413Y.0000000027

[15] Rappaz M, Drezet JM, Gremaud M (1999) A new hot-tearing criterion. Metall Mater Trans A Phys Metall Mater Sci 30:449–455. https://doi.org/10.1007/s11661-999-0334-z

[16] Li Y, Li H, Katgerman L, Du Q, Zhang J, Zhuang L (2020) Recent advances in hot tearing during casting of aluminium alloys. Prog Mater Sci. https://doi.org/10.1016/j.pmatsci.2020.100741

[17] Singer A, Jennings PH (1947) Hot-shortness of some aluminum-iron-silicon alloys of high purity. J Inst Met 73:273–284

[18] Shabestari SG, Moemeni H (2004) Effect of copper and solidification conditions on the microstructure and mechanical properties of Al–Si–Mg alloys. J Mater Process Technol 153–154:193–198. https://doi.org/10.1016/j.jmatprotec.2004.04.302

[19] Stanić D, Brodarac ZZ, Li L (2020) Influence of copper addition in AlSi7MgCu alloy on microstructure development and tensile strength improvement. Metals (Basel) 10:1–16. https://doi.org/10.3390/met10121623

[20] Guven Y, Hunt J (1988) Hot tearing in aluminium–copper alloys. Cast Met. https://doi.org/10.1080/09534962.1988.11818955

[21] Eskin DG, Katgerman L (2007) A quest for a new hot tearing criterion. Metall Mater Trans A Phys Metall Mater Sci A 38:1511–1519. https://doi.org/10.1007/s11661-007-9169-7

[22] Kamguo Kamga H, Larouche D, Bournane M, Rahem A (2010) Hot tearing of aluminum–copper B206 alloys with iron and silicon additions. Mater Sci Eng A 1:7413–7423. https://doi.org/10.1016/j.msea.2010.08.025

[23] Nagaumi H, Suzuki S, Okane T, Umeda T (2006) Effect of iron content on hot tearing of high-strength Al-Mg-Si alloy.

834 Mater Trans 47:2821–2827. https://doi.org/10.2320/matertra
835 ns.47.2821

[24] Kool WH, Katgerman L (2005) Hot tearing criteria evalua-
837 tion for direct-chill casting of an Al-4.5 pct Cu alloy. Metall
838 Mater Trans A Phys Metall Mater Sci 36:1537–1546. http
839 s://doi.org/10.1007/s11661-005-0245-6

[25] Kou S (2015) A criterion for cracking during solidification.
841 Acta Mater 88:366–374. https://doi.org/10.1016/j.actamat.2
842 015.01.034

[26] Song J, Pan F, Jiang B, Atrens A, Zhang MX, Lu Y (2016) A
844 review on hot tearing of magnesium alloys. J Magnes Alloy
845 4:151–172. https://doi.org/10.1016/j.jma.2016.08.003

[27] Won YM, Yeo TJ, Seol DJ, Kyu Hwan O (2000) A new
847 criterion for internal crack formation in continuously cast
848 steels. Metall Mater Trans B Process Metall Mater Process
849 Sci 31:779–794. https://doi.org/10.1007/s11663-000-0115-y

[28] Krbetschek C, Trân R, Wemme H, Ullmann M, Prahl U,
851 Rafaja D (2021) Hot crack susceptibility of cast
852 Mg97Y2Zn1. Eng Rep. https://doi.org/10.1002/eng2.12380

[29] Sweet L, Zhu SM, Gao SX, Taylor JA, Easton MA (2011)
854 The effect of iron content on the iron-containing inter-
855 metallic phases in a cast 6060 aluminum alloy. Metall Mater
856 Trans A Phys Metall Mater Sci 42:1737–1749. https://doi.
857 org/10.1007/s11661-010-0595-6

[30] Clyne TW, Kurz W (1981) Solute redistribution during
859 solidification with rapid solid state diffusion. Metall Trans A
860 Phys Metall Mater Sci A 12:965–971. https://doi.org/10.10
861 07/BF02643477

[31] Liu J, Kou S (2017) Susceptibility of ternary aluminum
863 alloys to cracking during solidification. Acta Mater
864 125:513–523. https://doi.org/10.1016/j.actamat.2016.12.028

[32] Rindler W, Kozeschnik E, Buchmayr B (2000) Computer
866 simulation of the brittle-temperature-range (BTR) for hot
867 cracking in steels. Steel Res 71:460–465. https://doi.org/10.
868 1002/srin.200005715

[33] Drezet JM, Allehaux D (2008) Application of the rappaz-
870 drezet-gremaud hot tearing criterion to welding of alu-
871 minium alloys. Hot Crack Phenom Welds I I:19–37. https://d
872 oi.org/10.1007/978-3-540-78628-3_2

[34] Sweet L, Easton MA, Taylor JA, Grandfield JF, Davidson
874 CJ, Lu L, Couper MJ, Stjohn DH (2013) Hot tear suscepti-
875 bility of Al-Mg-Si-Fe alloys with varying iron contents.
876 Metall Mater Trans A 44A:5396–5407. https://doi.org/10.1
877 007/s11661-012-1562-1

[35] Rakhmonov J, Qassem M, Larouche D, Liu K, Javidani M,
879 Chen X-G, Colbert J (2021) A new approach to determine
880 tensile stress–strain evolution in semi-solid state at near-
881 solidus temperature of aluminum alloys. Metals (Basel)
882 11:1–13

[36] Sutton M, Orteu J, Schreier H (2009) Image correlation for
884 shape, motion and deformation measurements

[37] Dong YL, Pan B (2017) A review of speckle pattern fabri-
886 cation and assessment for digital image correlation. Exp
887 Mech 57:1161–1181. https://doi.org/10.1007/s11340-017-0
888 283-1

[38] Stinville JC, Echlin MP, Texier D, Bridier F, Bocher P,
890 Pollock TM (2016) Sub-Grain scale digital image correlation
891 by electron microscopy for polycrystalline materials during
892 elastic and plastic deformation. Exp Mech 56:197–216. h
893 ttps://doi.org/10.1007/s11340-015-0083-4

[39] Weidmann E, Guesnier A (2008) Metallographic preparation
895 of aluminium and aliuminium alloys. Ballerup

[40] Chen XG, Langlais J (2000) Solidification behavior of
897 AA6111 automotive alloy. Mater Sci Forum 331:215–222. h
898 ttps://doi.org/10.4028/www.scientific.net/msf.331-337.215

[41] Larouche D (2007) Computation of solidification paths in
900 multiphase alloys with back-diffusion. Calphad Comput
901 Coupling Phase Diagr Thermochem 31:490–504. https://doi.
902 org/10.1016/j.calphad.2007.04.002

[42] Liu YL, Kang SB (1997) The solidification process of Al–
904 Mg–Si alloys. J Mater Sci 2:1443–1447

[43] Brito C, Costa TA, Vida TA, Bertelli F, Cheung N, Spinelli
906 JE, Garcia A (2015) Characterization of dendritic
907 microstructure, intermetallic phases, and hardness of direc-
908 tionally solidified Al-Mg and Al-Mg-Si alloys. Metall Mater
909 Trans A Phys Metall Mater Sci 46:3342–3355. https://doi.
910 org/10.1007/s11661-015-2967-4

[44] Kumar S, Grant PS, O'Reilly KAQ (2012) Fe bearing
912 intermetallic phase formation in a wrought Al-Mg-Si alloy.
913 Trans Indian Inst Met 65:553–557. https://doi.org/10.1007/
914 s12666-012-0221-y

[45] Wang ER, Hui XD, Chen GL (2011) Eutectic Al–Si–Cu–Fe–
916 Mn alloys with enhanced mechanical properties at room and
917 elevated temperature. Mater Des 32:4333–4340. https://doi.
918 org/10.1016/j.matdes.2011.04.005

[46] Hosford WF (2010) Mechanical behavior of materials.
920 Cambridge University Press, Cambridge

[47] Sih GC, Madenci E (1983) Crack growth resistance char-
922 acterized by the strain energy density function. Eng Fract
923 Mech 18:1159–1171. https://doi.org/10.1016/0013-7944(83
924)90008-5

[48] Gdoutos EE (2012) Crack growth instability studied by the
926 strain energy density theory. Arch Appl Mech
927 82:1361–1376. https://doi.org/10.1007/s00419-012-0690-9

[49] Mitchell JB, Cockcroft SL, Viano D, Davidson C, Stjohn D
929 (2007) Determination of strain during hot tearing by image
930 correlation. Metall Mater Trans A Phys Metall Mater Sci
931 38:2503–2512. https://doi.org/10.1007/s11661-007-9221-7

[50] Hu B, Li Z, Li D, Ying T, Zeng X, Ding W (2021) A hot tearing criterion based on solidification microstructure in cast alloys. J Mater Sci Technol 105:68–80. https://doi.org/10.1016/j.jmst.2021.06.071

[51] Cao G, Kou S (2006) Hot tearing of ternary Mg–Al–Ca alloy castings. Metall Mater Trans A Phys Metall Mater Sci 37:3647–3663. https://doi.org/10.1007/s11661-006-1059-x

[52] Vero J (1936) The hot shortness of aluminum alloys. Met Ind 48:431–442

[53] Easton M, Sweet L, Wang H, Grandfield J, Davidson CJ, Stjohn DH, Couper MJ (2012) Observation and prediction of the hot tear susceptibility of ternary Al-Si-Mg alloys. Metall Mater Trans A Phys Metall Mater Sci 43:3227–3238. https://doi.org/10.1007/s11661-012-1132-6

[54] Fabrègue D, Deschamps A, Suéry M, Poole WJ (2006) Rheological behavior of Al-Mg-Si-Cu alloys in the mushy state obtained by partial remelting and partial solidification at high cooling rate. Metall Mater Trans A Phys Metall Mater Sci 37:1459–1467. https://doi.org/10.1007/s11661-006-0090-2

[55] Adamiec J (2011) Assessment of high-temperature brittleness range of the casted alloy AZ91. Mater Sci Forum 690:41–44. https://doi.org/10.4028/www.scientific.net/MSF.690.41